Original scientific paper

LOAD PATH VISUALIZATION USING U* INDEX AND PRINCIPAL LOAD PATH DETERMINATION IN THIN-WALLED STRUCTURES

Shengjie Zhao, Luyue Mao, Nan Wu, Sviatoslaw Karnaoukh

Department of Mechanical Engineering, University of Manitoba, Winnipeg, Canada

ORCID iDs: Shengjie Zhao   https://orcid.org/0000-0002-1908-1133
           Luyue Mao   https://orcid.org/0009-0008-7283-4959
           Nan Wu   https://orcid.org/0000-0001-8768-1328
           Sviatoslaw Karnaoukh   https://orcid.org/0009-0005-0615-8874

Abstract. *U* index is used to express the load transfer inside a structure from a global perspective. Typically, a load path is defined as the ridgeline of the U* contours. However, it is cumbersome to directly locate the load paths by numerical approaches. This paper presents a streamline method with the fourth-order Runge-Kutta algorithm to visualize the load paths in thin-walled structures. The load paths can be consistently plotted on the surfaces of two-dimensional plates or three-dimensional shells by path projection. A new concept of principal load path is also introduced by evaluating the importance of load paths using statistical means. The principal load path is conceived as the "spine" of the structure that transfers the greatest internal force. A case study of a simplified vehicle body is presented. It is found that the structural stiffness can be greatly improved by reinforcing the set of principal load paths, which gives engineers an important insight into the development of weight-efficient structures.*

Key Words: *Load Path, Finite Element Analysis, Thin-walled Structures, Runge-Kutta Method*

1. INTRODUCTION

Load path analysis is an emerging technique in the field of structural design. It is essential to understand how the load transfers through a structure to properly arrange the material distribution, particularly with thin-walled structures [1]. Several theories and methods for load path analysis have been introduced by researchers and engineers. The concept of load flow proposed by Kelly et al. [2-4] is an early attempt to depict the load paths in a structure from the stress results. However, the stress concentration around holes and sharp corners can produce misleading information for load path visualization using this stress-based method [5]. Harasaki and Arora also proposed a new concept of transferred

force for load path analysis [6]. Load paths in a structure were indicated by the directions of transferred force vectors. A topology optimization algorithm was developed based on the magnitude of the transferred force [7,8]. Nonetheless, it is found that this method has low calculation efficiency and poor adaptability [9,10] compared to the stress-based methods.

The concept of U^* index [11] was developed and introduced by a group of Japanese researchers to describe the internal load transfer inside a structure. The U^* index theory originated from the concept of relative rigidity introduced by Takahashi [12]. The relative rigidity between an arbitrary point and the loading point can be expressed by the value of U^* index. The main load path in a structure was defined as the route with the highest relative rigidity. The reasonability of U^* index theory was experimentally validated by Pejhan et al. [13,14]. Three design criteria based on U^* index theory were also developed [11] and later applied to the applications of the structural design of vehicle components [15,16]. Besides, U^* index was recorded to be used in fiber trajectory optimization in composite structures [10,17], damage detection in thin-walled structures [18], and combination with other design methods, like bionic design [19]. Although the classic U^* index theory is based on linear elasticity, it can be extended to the analysis of nonlinear/plastic deformation cases by using the substitution modulus method [20] or altered U^* expression [21]. Several U^* variants (e.g., U^*_{sum} [22], U^{**} [23], and U^*_M [24]) were also introduced over the past decade to further extend the functionality of U^* index. Yet, the issue of low computation efficiency is also noticed from U^* load path analysis due to the iterative finite element (FE) calculations for nodal U^* values. To address this issue, Sakurai et al. [24] proposed an inspection loading method that decreases the calculation time by over 90% in large-scale models. This method prevents the FE calculations from reconstructing the stiffness matrix by converting multiple boundary conditions to multiple loading conditions. The applications of deep learning algorithms, such as the multilayer perceptron neural network built by Wang et. al [25] and the deep residual U-Net developed by Zhao et al. [26], further shorten the calculation time of U^* index.

While U^* index is promising in applications of structural analysis and design, there is no standardized procedure for visualizing the U^* load paths. According to the U^* index theory, a load path should follow the ridgeline of U^* contours from the loading point [11]. Yet it is tough to trace the load path by numerical methods without a specific objective function. Three approaches for load path visualization were identified in the literature. Vector plot is a straightforward approach to discretely visualize the internal force of a structure. It was used in early studies [2,6] of load path analysis, but it cannot create continuous load paths. The second approach is by using the load function developed by Tamijani et al. [27,28]. The load function is a scalar function using generalized Beltrami representation that can show the load paths with contour plots without post-processing. However, this function is only applicable to the load path theory introduced by Kelly et al. [2-4]. The third alternative for load path visualization is the streamline method, which is extensively used in tracing the fluid flow [29]. Kelly et al. implemented this method to visualize the load paths from the field of pointing stress vectors [30-32] with a fourth-order Runge-Kutta (RK4) algorithm. Even though the streamline plot is a more universal approach for vector field visualization, it is not directly feasible for U^* index as a scalar parameter. Moreover, the classic RK4 algorithm cannot guarantee the continuity of the load paths on curved surfaces, resulting in additional uncertainty in searching and visualizing successive load paths in thin-walled structures. An alternative approach is necessary to confine the visualized load paths on the surfaces of thin-walled structures without exiting the FE solution domain.

In this work, a methodology for U^* load path visualization in thin-walled structures is proposed. The load paths are represented by the streamlines derived from the gradient field of the U^* distribution. RK4 algorithm is used to increase the precision in streamline tracing. By using path projection, load paths can be efficiently plotted on the surfaces of two-dimensional (2D) plates and three-dimensional (3D) shells. A new concept of principal load path is also introduced to determine the most important route for global load transfer. Finally, a case study of a thin-walled vehicle body is provided to compare the importance of different load paths. Two sets of load paths in the vehicle structure are separately stiffened to evaluate their contributions to the structural stiffness. According to finite element analysis (FEA) and experimental tests, the reinforcement of the principal load paths is found to be more effective in reducing the total deformation. The method of load path visualization greatly helps the designers understand the internal load transfer inside a structure which is essential for the design of weight-efficient structures. Meanwhile, the concept of the principal load path provides the engineers with a simple solution to enhance the structural rigidity without further complicated analysis such as topology optimization.

2. U^* Index Theory

U^* index was derived from the concept of relative rigidity defined by Takahashi [11, 12]. Fig.1 (a) presents a linear elastic structure including an applied load at point A, a support at point B, and an arbitrary point C within the structure [11]. The internal stiffness between any two points is represented by the spring connection. The relationship among points A, B, and C considering three translational DOFs is expressed as:

$$\begin{bmatrix} P_A \\ P_B \\ P_C \end{bmatrix} = \begin{bmatrix} K_{AA} & K_{AB} & K_{AC} \\ K_{BA} & K_{BB} & K_{BC} \\ K_{CA} & K_{CB} & K_{CC} \end{bmatrix} \begin{bmatrix} D_A \\ D_B \\ D_C \end{bmatrix}. \tag{1}$$

K_{ij} ($i=A,B,C$; $j=A,B,C$) in Eq. (1) denotes the internal stiffness between points indicated by the subscripts. P_i and D_i ($i=A,B,C$) are the force and displacement vectors. Since point B is constrained in the original system, total strain energy U_P can be expressed as:
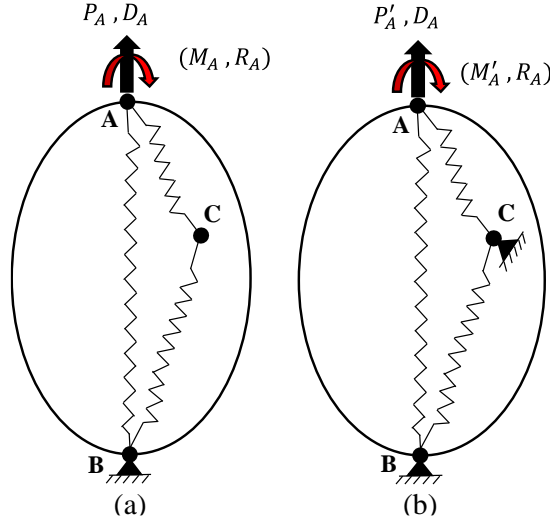
$$U_P = \frac{1}{2} P_A \cdot D_A = \frac{1}{2}(K_{AA}D_A + K_{AC}D_C) \cdot D_A \tag{2}$$

As shown in Fig. 1 (b), point C is also restrained in the modified system. Meanwhile, the displacement at point A is forced unchanged. Total strain energy U'_P stored in the modified system is expressed as:

$$U'_P = \frac{1}{2} P'_A \cdot D_A = \frac{1}{2}(K_{AA}D_A) \cdot D_A, \tag{3}$$

where P'_A denotes the applied load at point A in the modified system. Classic U^* index is then defined as [11]:

$$U^* = 1 - \frac{U_P}{U'_P}. \tag{4}$$

Fig. 1 Schematic diagram for U^* index calculation: (a) Original structure; (b) Modified structure [11, 23]

It can be rewritten by substituting Eqs. (2) and (3) into Eq. (4) [11]:

$$U^* = \left[1 - \frac{2U}{(K_{AC}D_C)} \cdot d_A\right]^{-1}. \tag{5}$$

The value of U^* ranges from 0 at point B to 1 at point A. It is observed from Eq. (5) that the U^* value is dependent on stiffness matrix K_{AC}. Therefore, it can be used to describe the connection strength between the arbitrary point and the loading point. For plates and shells that involve the rotational DOFs, the U^* index is formulated as [23]:

$$U^* = 1 - \frac{U_P + U_M}{U'_P + U'_M} = 1 - \frac{P_A \cdot D_A + M_A \cdot R_A}{P'_A \cdot D_A + M'_A \cdot R_A}, \tag{6}$$

where U_P, U_M are the external works of the original system by applied load P_A and bending moment M_A, and U'_P, U'_M are the external works of the modified system by applied load P'_A and bending moment M'_A. Fig. 2 depicts the U^* distribution of an example structure. The route that transfers the greatest loading is defined as the main load path. Stiffness decay vector β is hereby defined:

$$\beta = -\mathrm{grad}U^*. \tag{7}$$

The main load path highlighted as the bold line in Fig. 2 can be traced along the ridgeline of the U^* contours which has the smallest decay rate. However, since the magnitude of β is always zero along the U^* contour direction, the direction of the slowest U^* decay can be ambiguous. Also, in the occasion of more than one ridgeline, stiffness decay vector β may fail to locate the most important load path. Therefore, more efficient algorithms are demanded to automatically generate the load paths.
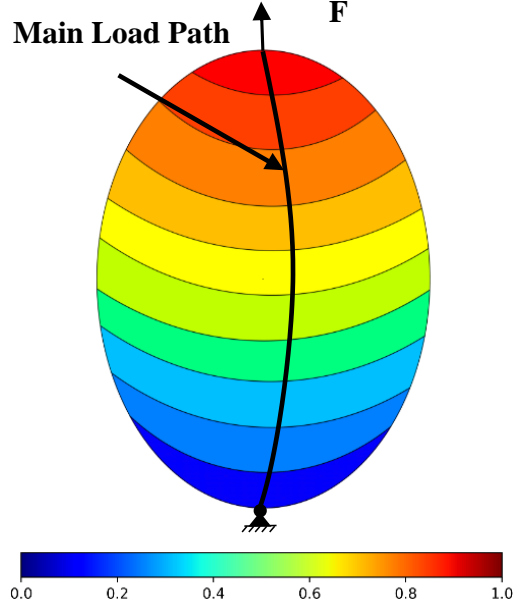
Fig. 2 Distribution of U^* values and main load path of a simple structure [11]

3. LOAD PATH VISUALIZATION METHODOLOGY

This section introduces a visualization methodology for U^* load paths by using the streamline approach. Ansys 2020 is used to perform the U^* load transfer analysis with a custom APDL script. The U^* distribution is then assigned to the FE model as a temperature field. The U^* gradient vector V at each node of the FE mesh can be acquired from the thermal gradient by thermal analysis. To successfully visualize the load paths represented by streamlines, instead of searching the slowest U^* descent direction from the loading point, the path plotting initiates from the supporting points by gradient ascent to find the local U^* maximum. The RK4 algorithm is used for locating the streamline points to reduce errors in path tracing. As illustrated in Fig. 3, given an initial point p_i on a plane, the new point p_{i+1} can be determined from:

$$dp_1 = V_N \Big|_{p_i} \Delta s,$$

$$dp_2 = V_N \Big|_{p_i + \frac{1}{2}dp_1} \Delta s,$$

$$dp_3 = V_N \Big|_{p_i + \frac{1}{2}dp_2} \Delta s, \tag{8}$$

$$dp_4 = V_N \Big|_{p_i + dp_3} \Delta s,$$

$$p_{i+1} = p_i + \frac{1}{6}(dp_1 + 2dp_2 + 2dp_3 + dp_4),$$

where Δs is the step size along the load path, and V_N is the normalized U^* gradient vector V with a direction of $\left(\dfrac{\partial U^*}{\partial x} i + \dfrac{\partial U^*}{\partial y} j + \dfrac{\partial U^*}{\partial z} k \right)$. Vector V_N can be specified at any location in the structure by interpolating the vector values at nearby nodes. A complete load path is generated by consecutively connecting the points from p_1 to p_N, where N is the total number of points.
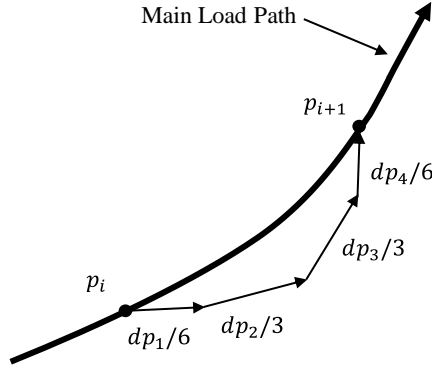
Fig. 3 Load path creation by Runge-Kutta sampling vectors

In 3D shell structures with curved surfaces, it is necessary to confine the load path within the solution domain [33]. One feasible approach is to project the load path segment onto the plane of its nearest element. Fig. 4. depicts the load path projection diagram for the determination of a new point p_{i+1} from initial point p_i in the orange element. p'_{i+1} is calculated first by the RK4 algorithm. The next step is to find the element that is closest to p'_{i+1}. Two vectors, $\vec{w}_1$ and $\vec{w}_2$, are subsequently defined by using any three nodes (N_1, N_2, and N_3) of the shell element in blue color. Unit normal vector $\vec{n}$ of this element can be calculated by the cross product of these two in-plane vectors:

$$\vec{n} = \frac{\vec{w}_1 \times \vec{w}_2}{\left| \vec{w}_1 \times \vec{w}_2 \right|}. \tag{9}$$

This normal vector intersects the targeted element at node N_2. By defining vector $\vec{q}$ from N_2 to p'_{i+1}, distance d from p'_{i+1} to the element can be calculated by:

$$d = \vec{q} \cdot \vec{n}. \tag{10}$$

Finally, the coordinate of new point p'_{i+1} can be obtained by:

$$\vec{q}' = \vec{q} - d\vec{n} ,$$
$$p'_{i+1} = N_2 + \vec{q}'. \tag{11}$$

A load path visualization example of a shell structure is presented in Fig. 5. This structure is constrained at two bottom corners while a horizontal force is applied at the center of the top edge. Two load paths are traced from the fixed points to the loading point

by the proposed methodology. Both load paths as displayed in red solid lines in symmetry perfectly lay on the surface of the shell structure. It can be seen that the load transfer conditions in thin-walled structures can be easily learned by the visualized load paths.
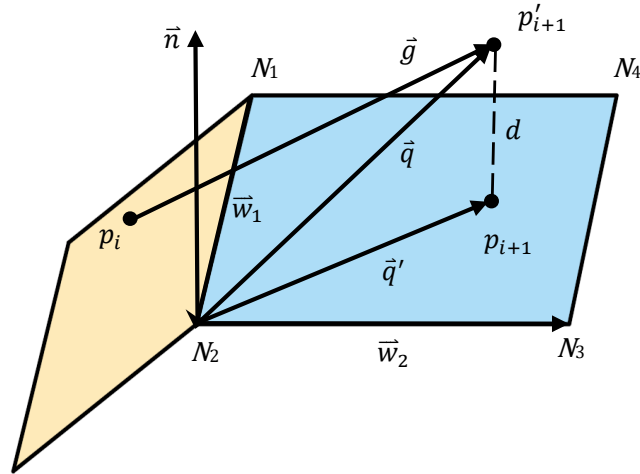

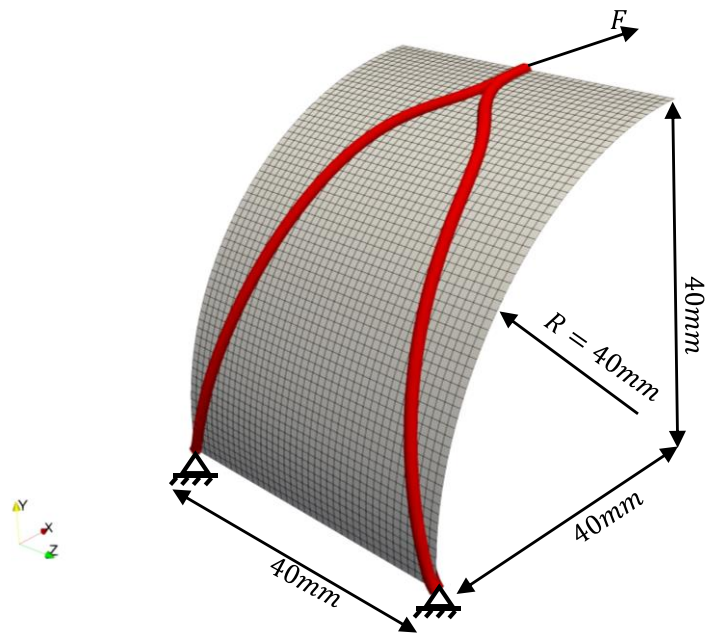**Fig. 4** Schematic diagram of vector projection

Fig. 5 Load path visualization in a shell structure

4. DETERMINATION OF PRINCIPAL LOAD PATH

There can be multiple load paths in some load cases, such as the example displayed in Fig. 5. It is essential to develop quantitative criteria to assess the importance of each main load path for load transfer. The load path with the greatest load transfer capability is called the principal load path. Three statistics measures are used to analyze the U^* distribution of the selected load path:

$$S_1 = \frac{\sum U^*}{N}. \tag{12}$$

$$S_2 = \begin{cases} U^*_{(N+1)/2} & \text{if } N \text{ is odd} \\ \dfrac{U^*_{N/2} + U^*_{(N+1)/2}}{2} & \text{if } N \text{ is even} \end{cases}. \tag{13}$$

$$S_3 = \sqrt{\frac{\sum(U^*_i - S_1)}{N}}. \tag{14}$$

where S_1, S_2, and S_3 represent the mean, median, and standard deviation of the U^* distribution along the load path. N is the total number of points on the path, and U^*_i is the U^* value at the i-th point. Since the U^* value describes the connection degree between an arbitrary point and the loading point, a load path with a great relative stiffness should have large mean and median values. Meanwhile, a smaller U^* standard deviation indicates a more consistent load transfer along the path with less force dispersion. Thereby, the principal load path in a structure can be determined by these three indicators.

**Table 1** Statistical measures for the load paths in the plate structure

	Mean, S_1	Median, S_2	Standard deviation, S_3
Load path 1	0.343	0.333	0.221
Load path 2	0.454	0.441	0.167
Load path 3	0.357	0.405	0.257

Table 2 Modified plate structures with reinforced load paths

	Load path element thickness (mm)	Plate model volume (mm^3)	Maximum deformation (mm)	Deformation reduction (%)
Original	3	7200	4.062eE-3	N/A
Load path 1	4	7378	3.739eE-3	7.948
Load path 2	4.483	7378	3.407eE-3	16.108
Load path 3	4.047	7378	3.848eE-3	5.275

To demonstrate the rationality of the quantitative criteria, a simple plate with a size of 60 mm × 40 mm and a uniform thickness of 3 mm is presented in Fig. 6 (a). Young's modulus of 210 GPa and Poisson's ratio of 0.3 are used in FE simulations. The left side

corners of the plate are constrained and a 100-N force along the *x*-axis is applied at the lower-right corner. Fig. 6 (b) presents the U^* distribution in this load case with two load paths in a solid black line and a dashed red line (Load Paths 1 and 2) automatically generated by the visualization methodology. It should be mentioned that Load Paths 1 and 2 are two separate load paths traced from the supporting points, even though their lower-right sections are closely located. Meanwhile, there are two apparent ridgelines noticed from the U^* map. One of them is identical to Load Path 1, and the other one is labeled

(a)

(b)
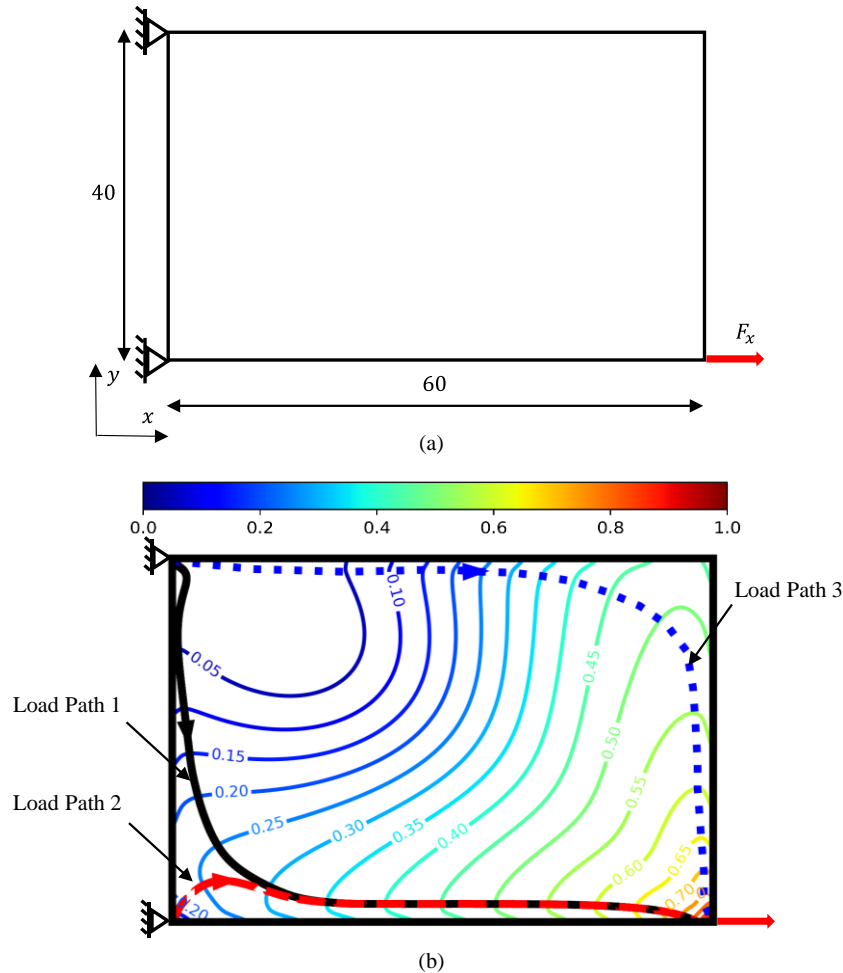
Fig. 6 Load path analysis on a plate structure: (a) Dimensions and boundary conditions of the plate; (b) Load paths inside the plate traced by streamlines (Load Paths 1 and 2) and ridgeline (Load Path 3)

as Load Path 3 in the blue dot line. The U^* decaying curves along these three load paths are drawn in Fig. 7, where *s* is the curvilinear coordinate along the load path starting from the loading point, and *l* is the length of the path. The statistical measures of the U^* distributions

are listed in Table 1. It is observed that Load Path 2 has the highest mean and median U^* value and the lowest standard deviation compared to the other two load paths. Meanwhile, Load Path 2 has the slowest decay rate as shown by the red dashed line in Fig. 7, indicating the great load-carrying capability of the load path. Given these data, Load Path 2 can be determined as the principal load path in this sample structure. An interesting finding is that the principal load path does not necessarily agree with U^* ridgelines, which are Load Paths 1 and 3 in this case.
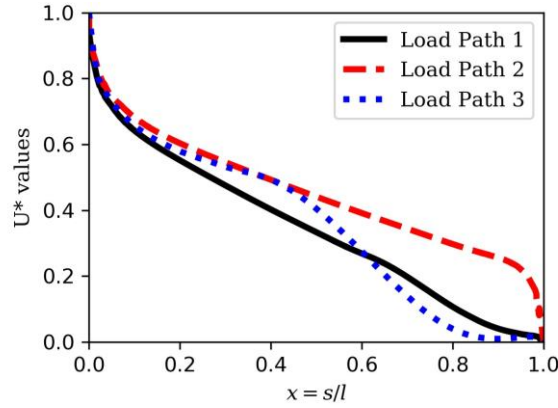

Fig. 7 U^* decay curves of the load paths in the plate

To further verify the load transfer efficiency of the principal load path, the plate in Fig. 6 is reinforced by respectively adding the same volume of materials (178 mm^3) on each load path. The stiffnesses of the enhanced structures are evaluated by their maximum displacements under the same loading condition. The thicknesses of the modified load paths and the deformation results by FEA are summarized in Table 2. As expected, reinforcing the principal load path (Load Path 2) offers the greatest deformation reduction rate of 16.11%, while the numbers for Load Paths 1 and 3 are 7.95% and 5.28%, respectively. It can be concluded that the members that have a great contribution to the structural stiffness can be effectively located by the principal load path. This is a promising feature for structural enhancement without changing the profile of the structure.

5. CASE STUDY

U^* index has been widely used in load path analysis on vehicle structures [15,16]. To further investigate the importance of the visualized load paths, a case study of a vehicle body is presented as displayed in Fig. 8. This miniature vehicle structure modeled by Shell181 elements is supported at the four corners on the back. A horizontal load of 156 N is evenly distributed on the front hoop. The same material properties as those of the previous plate example are used in FE simulations. The shell thickness of the original design is 1.6 mm. After calculating the U^* distribution, two sets of load paths are generated by implementing the RK4 algorithm on the U^* gradient field as shown in Fig. 8 (b). The U^* decay curves of both sets of load paths are drawn in Fig. 9. With a slower decay rate and

more desirable statistical properties listed in Table 3, Load Path Set 2 can be confidently defined as the principal path set. As discussed in Section 4, the principal load path reinforcement would offer a significant enhancement in structural stiffness. Followed by the same strategy, two modified designs with the same increased volume of 1169 mm^3 (7.5% over the original design) by separately thickening the elements on different sets of load paths are developed. The load path thickness arrangement and model volume of each design are provided in Table 4, where Org, LP1, and LP2 represent the original design and the modified designs with Load Path Sets 1 and 2 reinforcement, respectively. It is observed that the maximum displacement of the LP2 design is reduced by over 16% compared to that of the original design, while the reduction rate of the LP1 design is only 7.95%. With the same material usage, LP2 with the enhanced principal load paths leads to more significant stiffness improvement. These numerical results reaffirm the importance of the principal load path in structural design.
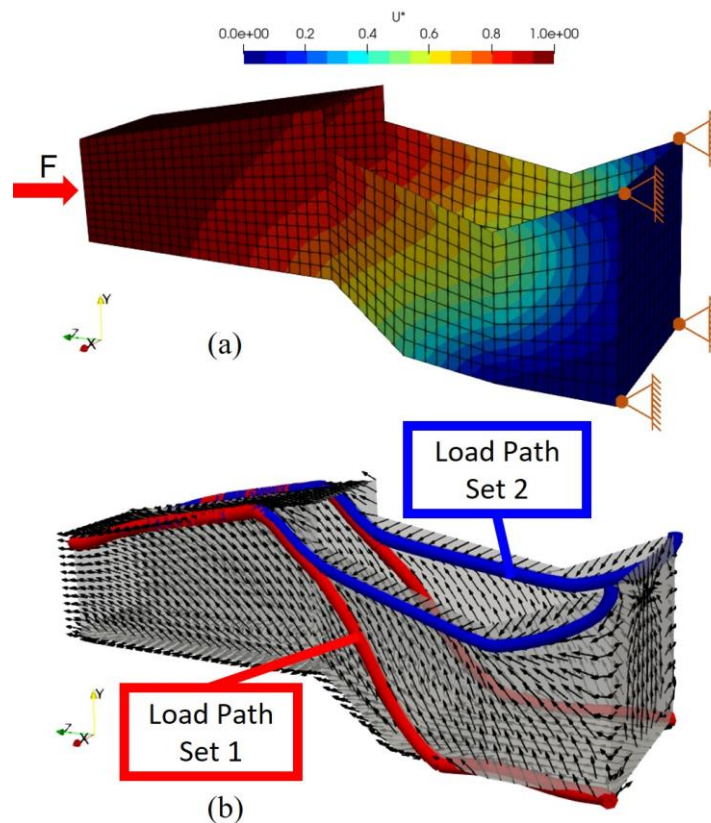

Fig. 8 *U** load path analysis of the thin-walled vehicle body: (a) *U** distribution; (b) Two sets of visualized load paths

Table 3 Statistical measures for the load paths in the vehicle body

|	Mean, S_1	Median, S_2	Standard deviation, S_3
Load Path Set 1	0.619	0.830	0.390
Load Path Set 2	0.761	0.903	0.271

Table 4 Modified designs with reinforced load paths

|	Load path element thickness (mm)	Shell model volume (mm^3)	Maximum deformation (mm)	Deformation reduction (%)
Org	1.6	1.556E+04	1.239eE-2	N/A
LP1	3.2	1.673E+04	1.227eE-2	7.948
LP2	3.072	1.673E+04	1.118eE-2	16.108
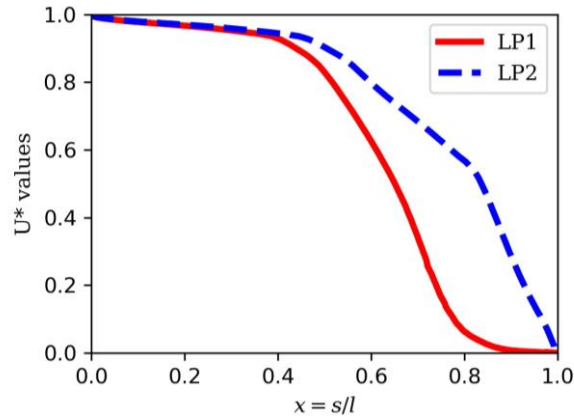
Fig. 9 U^* decay curves of the load paths in the vehicle body. LP1 and LP2 in this figure respectively denote the Load Path Sets 1 and 2 in the original design

Last but not least, the reinforced thin-walled structures are experimentally tested with 3D printed parts. The 3D printed specimens shown in Fig. 10 (a) are printed by Stereolithography (SLA) on a Formlab Form 3B using Tough 1500 Resin. Three specimens are prepared and tested for each design. The STL models for 3D printing are exported from Ansys Workbench. Four small cylinders are added to the supports of the STL models to avoid excessive constraints from the compression plate of the test machine. MTS Insight electromechanical testing system is used in this test with a 30 kN load cell. As presented in Fig. 10 (b), the specimen is subject to unidirectional compression to simulate the load case in the FEA. The design performance is evaluated by the specific stiffness in the linear region which is automatically extracted by the MTS testing software. The specific stiffness is calculated by the applied force divided by the vertical displacement. The force-displacement curves of each design are plotted in Fig. 11 (a) with different colors. The specific stiffness of the design is expressed by the bold solid line that takes the average slope of the regression lines from all three samples. The solid line of LP2 design has obviously the largest slope compared to the other two. Finally, the specific stiffness results are normalized by the case of the original design, and their comparison is provided in the bar graph of Fig. 11 (b). The enhancement of specific stiffness in LP2 design is 24.41%, while the result of LP1 design

is 14.61%. These test results again verify the importance gap between the principal load path and the secondary load path regarding the structural stiffness. This case study also showcases the potential of the load path visualization scheme in structural improvement. It offers the designers a clear picture of the load transfer inside a structure, and the principal load path can be directly used in design modification for better structural stiffness.
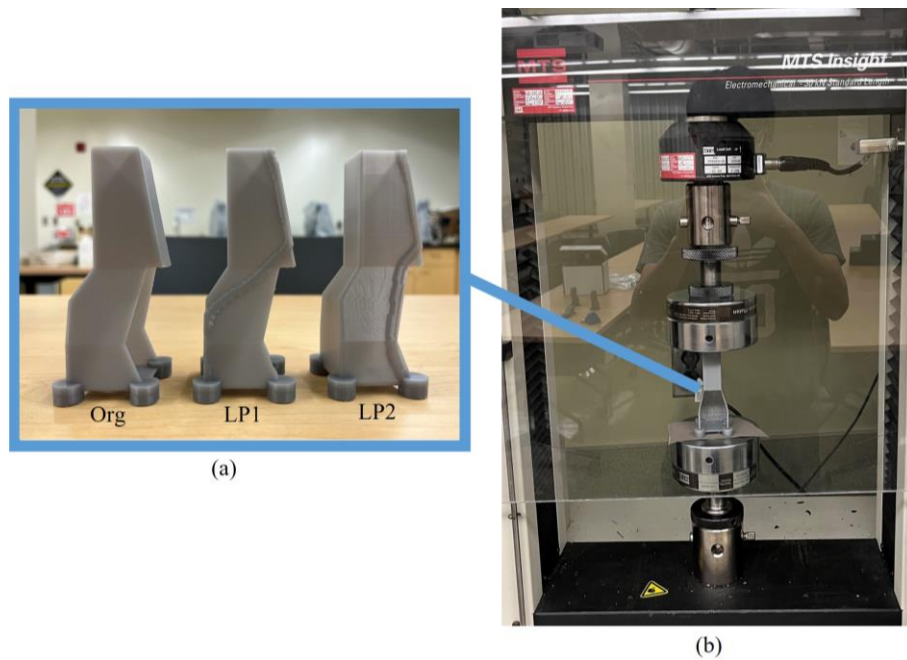
Fig. 10 Experimental tests: (a) 3D printed specimens; (b) Test setup on the MTS testing machine
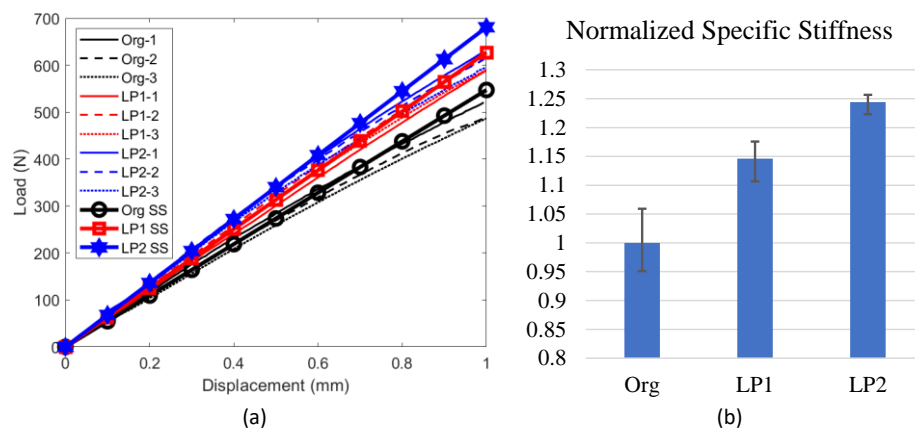
Fig. 11 Results of the compression tests: (a) Load-displacement curves, where SS denotes the fitted line with the slope of specific stiffness; (b) Normalized specific stiffness of different designs

6. CONCLUSIONS

This paper presents a methodology for U^* load path visualization in thin-walled structures using a streamline method with RK4 algorithm. A path projection scheme is introduced to reduce numerical errors and restrain the load paths on curved surfaces. The rationality of the visualization method and the importance difference among different load paths are investigated to define the principle load path. A case study of a simplified vehicle body is also provided to show the potential of the proposed methodology in structural enhancement. The major contributions and findings of this work can be summarized as follows:

- The numerical approach including the path projection scheme for U^* load path visualization in thin-walled structures is proposed for the first time.
- The importance difference among different load paths is numerically and experimentally investigated. Whereafter, a new definition of the principal load path is introduced.
- The direct reinforcement of the principal load path can significantly enhance the structural rigidity. It gives the designers a straightforward and effective solution in structural design modification and improvement.

While only the thin-walled structures are investigated for load path visualization in this study, the proposed methodology is also expected to work for 3D structures modeled with solid elements. It is worth noting that the accuracy of load paths also highly depends on the FE mesh. It can be a limitation as the computation cost of U* distribution for a large-scale model is tremendous. Meanwhile, while U* load path can effectively reveal the stiffness distribution of a structure, it overlooks the effect of stress concentration. Thereby, stress-based load paths would be recommended when it comes to local detailed design such as fiber path optimization in composites.

REFERENCES

1. Rama, G., Marinkovic, D., Zehn, M., 2018, *High performance 3-node shell element for linear and geometrically nonlinear analysis of composite laminates*, Composites Part B: Engineering, 151, pp. 118-126.
2. Kelly, D.W., Elsley, M., 1995, *A procedure for determining load paths in elastic continua*, Eng. Comput., 12, pp. 415-424.
3. Kelly, D.W., Tosh, M.W., 2000, *Interpreting load paths and stress trajectories in elasticity*, Eng. Comput., 17, pp. 117-135.
4. Kelly, D.W., Hsu, P., Asudullah, M., 2001, *Load paths and load flow in finite element analysis*, Eng. Comput., 18, pp. 303-313.
5. Naito, T., Kobayashi, H., Urushiyama, Y., Takahashi, K., 2011, *Introduction of new concept U* sum for evaluation of weight-efficient structure*, SAE International Journal of Passenger Cars-Electronic and Electrical Systems, 4, pp. 30-41.
6. Harasaki, H., Arora, J. S., 2001, *New concepts of transferred and potential transferred forces in structures*, Comput. Methods Appl. Mech. Eng., 191, pp. 385-406.
7. Harasaki, H., Arora, J., 2002, *Topology design based on transferred and potential transferred forces*, Structural and Multidisciplinary Optimization, 23, pp. 372-381.
8. Harasaki, H., Arora, J., 2001, *A new class of evolutionary methods based on the concept of transferred force for structural design*, Structural and Multidisciplinary Optimization, 22, pp. 35-56.

9. Marhadi, K., Venkataraman, S., 2009, *Comparison of quantitative and qualitative information provided by different structural load path definitions,* International Journal for Simulation and Multidisciplinary Design Optimization, 3, pp. 384-400.
10. Zhao, S., Wu, N., Wang, A.Q., 2021, *Load path-guided fiber trajectory in composite panels: A comparative study and a novel combined method,* Compos. Struct., 263, 113689.
11. Sakurai, T., Tanaka, J., Otani, A., Zhang, C., Takahashi, K., 2003, *Load Path Optimization and U* Structural Analysis for Passenger Car Compartments under Frontal Collision,* SAE Technical Paper Series, No. 2003-01-2734.
12. Takahashi, K., 1986, *Relative Rigidity of Structures and Saint Venant's Principle,* Japan Society of Mechanical Engineers, 52, pp. 2615-2621.
13. Pejhan, K., Wang, Q., Telichev, I., 2015, *Experimental study of U* index response to structural and loading variations*, ASME International Mechanical Engineering Congress and Exposition: American Society of Mechanical Engineers, V009T012A010.
14. Pejhan, K., Telichev, I., Wu, C.Q., Wang, Q., 2017, *Experimental validation of the U* index theory for load transfer analysis,* Int. J. Heavy Veh. Syst., 24, pp. 288-304.
15. Wang, Q., Pejhan, K., Telichev, I., Wu, C.Q., 2018, *Demonstration of the effectiveness of U*-based design criteria on vehicle structural design,* Proceedings of the Institution of Mechanical Engineers, Part D: Journal of Automobile Engineering, 232, pp. 995-1002.
16. Honda, M., Akima, S., Omiya, M., Takahashi, K., Sakurai, T., Maki, T., Nakagawa, K., 2018, *Optimization of Vehicle Body Local Structure Using Load Transfer Ustar (U*) Calculation,* Transactions of Society of Automotive Engineers of Japan, 49.6.
17. Suzuki, T., Fukushige, S., Tsunori, M., 2020, *Load path visualization and fiber trajectory optimization for additive manufacturing of composites,* Addit. Manuf., 31, 100942.
18. Zhao, S., Wu, N., Wang, Q., 2020, *Novel Damage Detection Tool Based on Load Path Analysis Using Ustar (U*),* IEEE Access, pp. 82607-82616.
19. Wu, F., Wang, Z., Song, D., Liang, H., 2022, *Lightweight design of control arm combining load path analysis and biological characteristics*, Reports in Mechanical Engineering, 3, pp. 71-82.
20. Wang, E.Y., Nohara, T., Ishii, H., Hoshino, H., Takahashi, K., 2011, *Load Transfer Analysis Using Indexes U* and U** for Truck Cab Structures in Initial Phase of Frontal Collision,* Advanced Materials Research, 156, pp. 1129-1140.
21. Wang, Q., Pejhan, K., Telichev, I., Wu, C.Q., 2017, *Extensions of the U* theory for applications on orthotropic composites and nonlinear elastic materials*, Int. J. Mech. Mater. Des., 13(3), pp. 469-480.
22. Naito, T., Kobayashi, H., Urushiyama, Y., Takahashi, K., 2011, *Introduction of new concept U*sum for evaluation of weight-efficient structure,* SAE Int. J. Passeng. Cars Electron. Electr. Syst., 4, pp. 30-41.
23. Wang, Q., Telichev, I., Wu, C.Q., 2018, *A new load transfer index (U*$_M$) with considering six degrees of freedom and its application in structural design and analysis,* Mechanics Based Design of Structures and Machines, 46, pp. 410-424.
24. Sakurai, T., Takahashi, K., Kawakami, H., Abe, M., 2007, *Reduction of calculation time for load path U* analysis of structures,* J. solid mech. mater. eng., 1, pp. 1322-1330.
25. Wang, Q., Zhang, G., Sun, C., Wu, N., 2019, *High efficient load paths analysis with U* index generated by deep learning,* Comput. Methods Appl. Mech. Eng., 344, pp. 499-511.
26. Zhao, S., Wu, N., Wang, Q., 2020, *Deep residual U-net with input of static structural responses for efficient U* load transfer path analysis,* Adv. Eng. Inform., 46, 101184.
27. Tamijani, A.Y., Hurley, J., Gharibi, K., 2018, *Determination of load paths in plates and shells,* Thin-Walled Structures, 127, pp. 646-653.
28. Tamijani, A.Y., Gharibi, K., Kobayashi, M.H., Kolonay, R.M., 2018, *Load paths visualization in plane elasticity using load function method,* International Journal of Solids and Structures, 135, pp. 99-109.
29. Giles, M., Haimes, R., 1990, *Advanced interactive visualization for CFD,* Computing Systems in Engineering, 1, pp. 51-62.
30. Kelly, D., Pearce, G., Schroder-Turner, K., 2019, *Plotting Load Paths from Finite Element Stress Results for Aerospace Structures*, AIAA Scitech 2019 Forum*, 0509
31. Kelly, D., Reidsema C., Bassandeh, A., Pearce, G., Lee, M., 2011, *On interpreting load paths and identifying a load bearing topology from finite element analysis,* Finite Elements in Analysis and Design, 47, pp. 867-876.
32. Kelly, D.W., Reidsema C.A., Lee, M.C.W., 2011, *An algorithm for defining load paths and a load bearing topology in finite element analysis,* Eng. Comput. (Swansea), 28, pp. 196-214.